Ferrimagnetic resonance induced by the spin Hall effect

Chi Sun [ORCID],[*] Hyunsoo Yang [ORCID], and Mansoor B. A. Jalil[†]

Department of Electrical and Computer Engineering, National University of Singapore, 117576 Singapore

A bilayer consisting of a ferrimagnetic insulator (FiM) and a heavy metal (HM) can be used as a "pump-probe" system to analyze the magnetic properties of the FiM. An oscillating electric current in the HM induces spin current injection into the FiM via the spin Hall effect. The resulting magnetization dynamics of the FiM, in turn, causes spin pumping back into the HM and modifies its conductivity via the inverse spin Hall effect (ISHE). We present a phenomenological theory to model the ISHE output spectrum, in which the Landau-Lifshitz-Gilbert equations governing the FiM dynamics are coupled to the spin-diffusion equations governing the spin and charge transports in the HM. It is found that the ISHE signal is greatly enhanced at the magnetization compensation point of the FiM. Furthermore, the peak frequencies and amplitudes of the ISHE spectrum are strongly correlated to the magnetic properties of the FiM sublattices. Most interestingly, the ISHE output can be increased by several orders of magnitude by tuning the on-site-sublattice and cross-sublattice damping constants. Our analysis shows the possibility of using the FiM/HM bilayer system as a sensitive probe into the magnetic parameters of the FiM sublattices. Conversely, the drastically enhanced ISHE signal with appropriate tuning of the damping parameters suggests a means to substantially improve the spin torque efficiency in FiM-based heterostructures.

I. INTRODUCTION

The interconversion between charge and spin currents forms the foundation of spintronics, and this can be achieved efficiently through the spin Hall effect (SHE) and its counterpart, the inverse spin Hall effect (ISHE), in nonmagnetic heavy metals (HMs) with strong spin-orbit coupling (SOC) such as platinum (Pt), tantalum (Ta), and tungsten (W) [1–4]. These two phenomena, the SHE and ISHE, can be combined in a coupled bilayer system consisting of a HM layer and a magnetic insulator (MI) layer, to yield the so-called spin Hall magnetoresistance (SMR) [5–7]. This is essentially a "pump-probe" system where an oscillating electric current is applied to the HM layer, which excites the magnetization dynamics in the MI via SHE. This, in turn, induces a back-reaction on the HM layer via the ISHE, and the resulting SMR output can be used to probe the magnetization dynamics of the MI. This SMR-induced spin-torque ferromagnetic resonance (ST-FMR) measurement was theoretically proposed by Chiba *et al.* [8] and then experimentally demonstrated [9–12].

Recently, antiferromagnetic materials (AFMs) with compensated magnetic moments and fast intrinsic magnetization dynamics have attracted intensive research interests [13–17]. Compared with AFMs, ferrimagnetic materials (FiMs) allow further manipulation of magnetic states since their magnetization is electrically detectable and can be modified by changing the sublattice element concentration [18–20] or temperature [21,22]. Furthermore, FiMs possess distinct properties near their compensation point, e.g., enhanced spin torque effi-

ciency [18,23], fast current-driven domain walls [24], and small skyrmions [21], etc., which are potentially useful for applications. Insulating FiMs have also been intensively studied in conjunction with spin transports [25–27].

Combining the themes of SMR and FiM, we propose a bilayer system consisting of a FiM insulator and a HM (see Fig. 1), as a means to investigate the unique magnetization dynamics of FiM. Under application of an oscillating electric current in the HM, an oscillating transverse spin current is generated via SHE which then exerts an oscillating spin torque on the FiM. This induces the magnetization precession at the FMR frequency, which in turn propagates a spin current back to the HM through spin pumping. Consequently, through the ISHE, the resultant spin current can be transferred to a detectable electrical signal, which gives information of the current-induced magnetization dynamics in the FiM. This broadly shares the principle of the SMR-induced ST-FMR measurement.

Here we present a phenomenological theory to investigate the ISHE signal output (i.e., effective change in the electric conductivity of the HM). We solve the coupled spin-diffusion equations, which model the SHE and ISHE in the HM, with the Landau-Lifshitz-Gilbert (LLG) equations describing the FiM magnetization dynamics. As expected, we showed the large enhancement of the ISHE signal at the magnetization compensation point of the FiM. In general, there are two macrospin resonance peaks in the ISHE signal, and the peak frequencies and relative amplitudes can be correlated to the magnetization properties of the FiM sublattices. More interestingly, the asymmetry of the damping constants gives rise to distinct features in the resonance spectrum. In particular, the cross-sublattice damping can be tuned to enhance the ISHE signal by several orders of magnitude. Our results indicate that
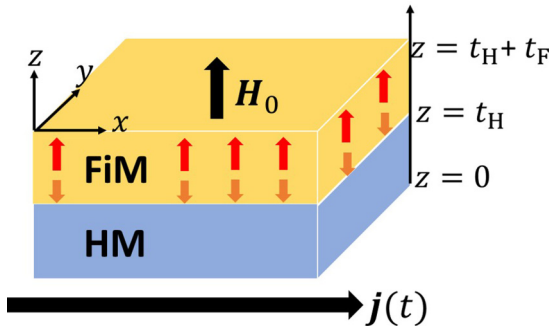
* e0021580@u.nus.edu
† elembaj@nus.edu.sg

FIG. 1. Diagram of the FiM/HM structure in this work. The oscillating electric current $\boldsymbol{j}(t)$ is applied along the x direction. Here we consider the FiM with perpendicular magnetization anisotropy (PMA), and the static magnetic field $\boldsymbol{H}_0$ is applied along its easy-axis (i.e., the z axis). $t_{H(F)}$ is the thickness of the HM (FiM).

the coupled FiM/HM bilayer is a sensitive system to probe the magnetic properties of FiM and distinguish its sublattice contributions. Conversely, the bilayer system could also be utilized to achieve enhanced and controllable spin torque efficiency in FiM layers.

II. THEORY AND MODEL

Figure 1 is the diagram of the FiM/HM structure in this work, where the oscillating electric current density $\boldsymbol{j}(t)$ is applied along the x direction, i.e., $\boldsymbol{j}(t) = j_0 e^{i\omega t}\hat{\boldsymbol{x}}$ with frequency $\omega = 2\pi f$. Since the FiM layer is insulating, $\boldsymbol{j}(t)$ flows exclusively within the HM. In the following, we use subscripts H and F to represent the quantities within the HM and the FiM layers, respectively.

A. Spin diffusion in the HM

We begin by considering the spin accumulation $\boldsymbol{\mu}_{s,H}$ in the HM induced by the oscillating electric current. The spin accumulation is described by the spin-diffusion equation

$$\partial_t \boldsymbol{\mu}_{s,H} = D\partial_z^2 \boldsymbol{\mu}_{s,H} - \frac{\boldsymbol{\mu}_{s,H}}{\tau_{sf}}, \qquad (1)$$

where D is the diffusion constant and τ_{sf} is the spin-flip relaxation time. In the frequency domain, the general solution of the spin accumulation reads [8]

$$\boldsymbol{\mu}_{s,H}(z, \omega) = \boldsymbol{A}(\omega)\exp[\kappa(\omega)z] + \boldsymbol{B}(\omega)\exp[-\kappa(\omega)z], \qquad (2)$$

where $\kappa(\omega) = \sqrt{1 - i\omega\tau_{sf}}/\lambda_H$ refers to the inverse of the frequency-dependent spin diffusion length with the general spin-diffusion length $\lambda_H = \sqrt{D\tau_{sf}}$. $\boldsymbol{A}(\omega)$ and $\boldsymbol{B}(\omega)$ are the constant column vectors to be determined by applying appropriate boundary conditions. The frequency-dependent spin current density consists of the diffusion and SHE contributions, i.e.,

$$\boldsymbol{j}_{s,H}(z, \omega) = -\frac{\sigma_H(\omega)}{e}\partial_z \boldsymbol{\mu}_{s,H}(z, \omega) + \theta_{sH}\sigma_H(\omega)E(\omega)\hat{\boldsymbol{y}}, \qquad (3)$$

where $\sigma_H(\omega) = \frac{\sigma_{H,0}}{1-i\omega\tau_{sf}}$ is the complex frequency-dependent conductivity and $E(\omega)$ is the electric field associated with the applied oscillating current density $j(\omega) = \sigma_H(\omega)E(\omega)$ in the frequency domain. $\theta_{sH}j(\omega)$ gives the transverse pure spin Hall

current polarized along $\hat{\boldsymbol{y}}$, where θ_{sH} is the spin Hall angle. $e = |e|$ is the electron charge.

Here we introduce the interfacial spin current density $\boldsymbol{Q}^{F\to H}$ at the FiM/HM interface ($z = t_H$), which is defined as being injected from the FiM to the HM, i.e., $\boldsymbol{j}_{s,H}(t_H, \omega) = -\boldsymbol{Q}^{F\to H}$. For notational simplicity, this interfacial spin current density is denoted as $\boldsymbol{Q}$ in the following. By applying the boundary condition that the spin current density vanishes at the outer boundary, i.e., $\boldsymbol{j}_{s,H}(0, \omega) = 0$, the spin accumulation in the HM can be solved from the aforementioned drift-diffusion equation in terms of $\boldsymbol{Q}$ as

$$\boldsymbol{\mu}_{s,H}(z, \omega) = \frac{e}{\kappa(\omega)\sigma_H(\omega)}\text{csch}[t_H\kappa(\omega)](\cosh[\kappa(\omega)z]\boldsymbol{Q}$$
$$+ \theta_{sH}\sigma_H(\omega)E(\omega)\{\cosh[\kappa(\omega)z]$$
$$- \cosh[\kappa(\omega)(t_H - z)]\}\hat{\boldsymbol{y}}). \qquad (4)$$

Accordingly, the spin accumulation at the FiM/HM interface ($z = t_H$) on the HM side is given by

$$\boldsymbol{\mu}_{s,H}(t_H, \omega) = \frac{e}{\kappa(\omega)\sigma_H(\omega)}\left\{\coth[t_H\kappa(\omega)]\boldsymbol{Q}\right.$$
$$\left. + \tanh\left[\frac{t_H\kappa(\omega)}{2}\right]\theta_{sH}\sigma_H(\omega)E(\omega)\hat{\boldsymbol{y}}\right\}. \qquad (5)$$

The value of $\boldsymbol{Q}$ in the relation above is yet to be determined. Note that $\boldsymbol{Q}$ is the quantity that links the spin transport in the HM with the magnetization dynamics in the FiM. We shall see later that it would be affected by the spin pumping back current induced by the FiM dynamics.

B. Magnetization dynamics in the FiM

The oscillating spin current generated in the HM via SHE exerts spin torques on the adjacent FiM, thereby exciting its magnetization dynamics. Here we utilize a two-sublattice model with distinct parameters for each sublattice in the FiM. Consider the two coupled LLG equations for the two sublattices ($i = 1, 2$),

$$\frac{d\boldsymbol{m}_1}{dt} = -\gamma_1\mu_0\boldsymbol{m}_1 \times \boldsymbol{H}_1 + \alpha_{11}\boldsymbol{m}_1 \times \frac{d\boldsymbol{m}_1}{dt}$$
$$+ \alpha_{12}\boldsymbol{m}_1 \times \frac{d\boldsymbol{m}_2}{dt} + T_1\boldsymbol{\tau}_1$$
$$\frac{d\boldsymbol{m}_2}{dt} = -\gamma_2\mu_0\boldsymbol{m}_2 \times \boldsymbol{H}_2 + \alpha_{22}\boldsymbol{m}_2 \times \frac{d\boldsymbol{m}_2}{dt}$$
$$+ \alpha_{21}\boldsymbol{m}_2 \times \frac{d\boldsymbol{m}_1}{dt} + T_2\boldsymbol{\tau}_2, \qquad (6)$$

where $\boldsymbol{m}_i$ and γ_i denote the sublattice magnetization unit vector and gyromagnetic ratio, respectively. μ_0 is the vacuum permeability. The first term on the right-hand side of Eq. (6) represents the precession term with respect to the sublattice effective field $\boldsymbol{H}_i$. The following two terms pertain to the damping effect in the system. In addition to the damping constant for the on-site-sublattice (i.e., α_{11} and α_{22}); we also include the cross-sublattice terms in the Gilbert damping [28], i.e., α_{12} and α_{21}. The last term gives the spin torque contribution, where $\boldsymbol{\tau}_i = \boldsymbol{m}_i \times (\boldsymbol{m}_i \times \boldsymbol{Q})$ is the spin torque exerted on

sublattice i with the coefficient $T_i = \frac{\hbar}{2e} \frac{\gamma_i}{M_{i0}t_F}$. Note that $\boldsymbol{\tau}_i$ is produced by the spin current $\boldsymbol{Q}$ injected into the FiM from the HM. M_{i0} is the saturation magnetization of sublattice i. The free-energy density of the FiM has the form

$$F = -\mu_0 \boldsymbol{H}_{\text{ex}} \cdot (\boldsymbol{M}_1 + \boldsymbol{M}_2) - K_1 (\boldsymbol{M}_1 \cdot \hat{\boldsymbol{z}})^2$$
$$- K_2 (\boldsymbol{M}_2 \cdot \hat{\boldsymbol{z}})^2 + J_{\text{ex}} \boldsymbol{M}_1 \cdot \boldsymbol{M}_2, \tag{7}$$

where $\boldsymbol{M}_i = M_{i0}\boldsymbol{m}_i$ and $\boldsymbol{H}_{\text{ex}} = \boldsymbol{H}_0 + \boldsymbol{h}_{\text{Oe}}$ with $\boldsymbol{H}_0 = H_0\hat{\boldsymbol{z}}$ and $\boldsymbol{h}_{\text{Oe}} = h_{\text{Oe}}\hat{\boldsymbol{y}}$. $\boldsymbol{H}_0$ represents the external static magnetic field and $\boldsymbol{h}_{\text{Oe}}$ is the Oersted field induced by the applied oscillating electric current. K_i and J_{ex} describe the anisotropy and exchange energy terms, respectively. Note that $\boldsymbol{H}_0$ is applied along the easy axis of the FiM, i.e., we are considering the FiM possessing perpendicular magnetization anisotropy (PMA). Consequently, the sublattice effective field is obtained from $\boldsymbol{H}_i = -\frac{1}{\mu_0} \frac{\partial F}{\partial \boldsymbol{M}_i}$ as

$$\boldsymbol{H}_i = \boldsymbol{H}_{\text{ex}} + \frac{2K_i}{\mu_0} M_{iz}\hat{\boldsymbol{z}} - \frac{J_{\text{ex}}}{\mu_0} \boldsymbol{M}_j \tag{8}$$

with $(i, j) = (1, 2)$ or $(2, 1)$. $M_{iz} = M_{i0}m_{iz}$ and m_{iz} is the z component of $\boldsymbol{m}_i$. Here we are interested in the small-angle precession of the magnetizations, i.e., only the first-order deviations from the ground state of magnetizations are considered. Therefore, it is assumed that the lattice magnetizations are largely oriented along the external static field $\boldsymbol{H}_0$, i.e., $\boldsymbol{m}_1 = m_{1x}\hat{\boldsymbol{x}} + m_{1y}\hat{\boldsymbol{y}} + \hat{\boldsymbol{z}}$ and $\boldsymbol{m}_2 = m_{2x}\hat{\boldsymbol{x}} + m_{2y}\hat{\boldsymbol{y}} - \hat{\boldsymbol{z}}$. Note this assumption also applies in the absence of $\boldsymbol{H}_0$ as a result of the PMA in the FiM. In this small-angle limit, the LLG equations can be linearized as

$$\mathcal{M}\boldsymbol{m} = h_{\text{Oe}}\mathcal{L} + \mathcal{R}\boldsymbol{Q}, \tag{9}$$

where $\boldsymbol{m} = (m_{1x}, m_{1y}, m_{2x}, m_{2y})^T$ and $\boldsymbol{Q} = (Q_x, Q_y)^T$. The matrices in Eq. (9) are explicitly given by

$$\mathcal{M} = \begin{pmatrix} i\omega & \omega_{1\text{eff}} + i\alpha_{11}\omega & 0 & \omega_{12} + i\alpha_{12}\omega \\ -\omega_{1\text{eff}} - i\alpha_{11}\omega & i\omega & -\omega_{12} - i\alpha_{12}\omega & 0 \\ 0 & -\omega_{21} - i\alpha_{21}\omega & i\omega & -\omega_{2\text{eff}} - i\alpha_{22}\omega \\ \omega_{21} + i\alpha_{21}\omega & 0 & \omega_{2\text{eff}} + i\alpha_{22}\omega & i\omega \end{pmatrix}, \tag{10}$$

$$\mathcal{L} = \mu_0(\gamma_1 \quad 0 \quad -\gamma_2 \quad 0)^T, \tag{11}$$

and

$$\mathcal{R} = -\begin{pmatrix} T_1 & 0 & T_2 & 0 \\ 0 & T_1 & 0 & T_2 \end{pmatrix}^T, \tag{12}$$

where we have introduced the frequency terms $\omega_{1\text{eff}} = \gamma_1(2K_1M_{10} + J_{\text{ex}}M_{20} + \mu_0 H_0)$, $\omega_{2\text{eff}} = \gamma_2(2K_2M_{20} + J_{\text{ex}}M_{10} - \mu_0 H_0)$, $\omega_{12} = \gamma_1 J_{\text{ex}}M_{20}$, and $\omega_{21} = \gamma_2 J_{\text{ex}}M_{10}$. By setting the determinant of $\mathcal{M}$ as zero, the complex eigenfrequencies of ω can be obtained, in which the real components correspond to the resonant frequency ω_{res} and the imaginary components describe the damping of the corresponding modes. If the damping of the system is assumed to be sufficiently small as to not affect the resonance frequency significantly, the resonance frequency ω_{res} can be expressed as

$$\omega_{\text{res}} = \frac{1}{2}\left[\sqrt{(\omega_{1\text{eff}} + \omega_{2\text{eff}})^2 - 4\omega_{12}\omega_{21}} \pm (\omega_{1\text{eff}} - \omega_{2\text{eff}})\right]. \tag{13}$$

From the above, we observe that the FiM exhibits two macrospin resonance frequencies. The two resonance modes agree with the earlier theoretical descriptions [29,30], and they are usually called the ferromagnetic mode (for the low frequency) and the exchange mode (for the high frequency). The assumption of negligible dependence of ω_{res} on the damping parameters will be validated in subsequent numerical simulations.

C. Interfacial currents and the ISHE-induced electric conductivity

At the FiM/HM interface, the spin current density consists of spin transfer and spin pumping contributions [31], i.e.,

$$\boldsymbol{J}_s^{\text{STT}}(t) = \frac{G_r}{2e} \sum_i \boldsymbol{m}_i \times [\boldsymbol{m}_i \times \boldsymbol{\mu}_{s,\text{H}}(t_{\text{H}})], \tag{14}$$

$$\boldsymbol{J}_s^{\text{SP}}(t) = \frac{\hbar G_r}{2e} \sum_i \boldsymbol{m}_i \times \frac{d\boldsymbol{m}_i}{dt}, \tag{15}$$

where G_r is the interfacial mixing conductance for both sublattices (i.e., $G_{11} = G_{22} = G_r$) and the cross-sublattice terms [28,32] are neglected for simplicity (i.e., $G_{12} = G_{21} = 0$). In the frequency domain to the first order, we have

$$\boldsymbol{Q} = \boldsymbol{J}_s^{\text{STT}}(\omega) + \boldsymbol{J}_s^{\text{SP}}(\omega) \tag{16}$$

with

$$\boldsymbol{J}_s^{\text{STT}}(\omega) = -\frac{G_r}{e} \boldsymbol{\mu}_{s,\text{H}}(t_{\text{H}}, \omega) \tag{17}$$

and

$$\boldsymbol{J}_s^{\text{SP}}(\omega) = \frac{\hbar G_r}{2e} \mathcal{H}\mathcal{M}^{-1}[h_{\text{Oe}}(\omega)\mathcal{L} + \mathcal{R}\boldsymbol{Q}], \tag{18}$$

where

$$\mathcal{H} = i\omega \begin{pmatrix} 0 & -1 & 0 & 1 \\ 1 & 0 & -1 & 0 \end{pmatrix}. \tag{19}$$

The Oersted field is determined by Ampère's law as $h_{\text{Oe}}(\omega) = \frac{\sigma_H(\omega)E(\omega)t_H}{c}$, where c is the speed of light [8]. Note that Eq. (18) captures the back current into the HM layer due to the spin pumping induced by the FiM dynamics. The FiM dynamics is obtained by considering Eq. (9) and taking the time derivative. Thus, as seen from Eq. (16), the interfacial current $\boldsymbol{Q}$ consists of the contributions from the SHE induced by the original source of excitation, the oscillating electric current, and that of the spin-pumped back current from the FiM. Combining Eqs. (16)–(18), the interfacial spin current density $\boldsymbol{Q}$ can be solved as

$$\boldsymbol{Q} = -\frac{\tanh\left[\frac{t_H\kappa(\omega)}{2}\right]}{\kappa(\omega)}\theta_{\text{sH}}G_r E(\omega)\boldsymbol{\mathcal{F}}^{-1}\hat{\boldsymbol{y}}, \quad (20)$$

where

$$\boldsymbol{\mathcal{F}} = \left(1 + \frac{G_r}{\kappa(\omega)\sigma_H(\omega)}\coth\left[t_H\kappa(\omega)\right]\right)\mathbf{I}_2 - \frac{\hbar G_r}{2e}\boldsymbol{\mathcal{H}}\boldsymbol{\mathcal{M}}^{-1}\boldsymbol{\mathcal{R}}, \quad (21)$$

with $\mathbf{I}_2$ representing the 2×2 identity matrix. Note we have omitted the Oersted field contribution in Eqs. (20) and (21). It can be easily seen from Eq. (20) that $\boldsymbol{Q} \propto \theta_{\text{sH}}E(\omega)$, i.e., the pure spin current density generated directly through the SHE.

In the SMR mechanism, the spin current is generated by the SHE from the applied oscillating electric current and can be detected by the ISHE through the measurement of the modified electric current or voltage in the HM. The total longitudinal electric current density (along $\hat{\boldsymbol{x}}$) reads [5]

$$j_{cx,H}(z, \omega) = \sigma_H(\omega)E(\omega) - \frac{\sigma_H(\omega)}{e}\theta_{\text{sH}}\partial_z\mu_{sy,H}(z, \omega), \quad (22)$$

where $\mu_{sy,H}$ denotes the y component of $\boldsymbol{\mu}_{s,H}$. In the above, the expression for the ISHE-induced current is obtained by incorporating the solution for $\boldsymbol{Q}$ in Eq. (20) into the expression for $\mu_{sy,H}$ in Eq. (4), and then substituting the latter in Eq. (22). Further, we average the electric current density over the HM layer thickness [i.e., $j_{cx,H}(\omega) = \frac{1}{t_H}\int_0^{t_H} j_{cx,H}(z, \omega)dz$], so that the effective electric conductivity change $\Delta\tilde{\sigma}_H(\omega)$ modified by the ISHE can be obtained as

$$\frac{\Delta\tilde{\sigma}_H(\omega)}{\sigma_H(\omega)} = -\frac{\theta_{\text{sH}}}{t_H\kappa(\omega)}\frac{\tanh\left[\frac{t_H\kappa(\omega)}{2}\right]}{E(\omega)}Q_y$$
$$= \frac{\theta_{\text{sH}}^2 G_r}{t_H\kappa^2(\omega)}\tanh^2\left[\frac{t_H\kappa(\omega)}{2}\right](\boldsymbol{\mathcal{F}}^{-1}\hat{\boldsymbol{y}})_y, \quad (23)$$

where Q_y denotes the y component of $\boldsymbol{Q}$, which is given by Eq. (20). Equation (23) is our final analytical result and it encapsulates the SMR output signal that is dependent on the FiM dynamics which is, in turn, induced by the initial oscillating electric current. From Eq. (23), it can be seen that the detected signal change is proportional to the interfacial spin current density (e.g., Q_y), and therefore it is in the second order of θ_{sH}.

III. NUMERICAL SIMULATION AND DISCUSSION

In this section, we examine the ISHE-induced output signal [i.e., effective electric conductivity change of the HM given by Eq. (23)] as a probe into the magnetic properties of the FiM. The parameters employed in the numerical simulations are (i) in the HM made of Pt [33,34]: $\sigma_{H,0} = 2.44 \times 10^6\ \Omega^{-1}\text{m}^{-1}$, $\lambda_H = 1.4$ nm, $\tau_{\text{sf}} = 10$ fs, and $\theta_{\text{sH}} = 0.12$; (ii) in the FiM [28]: $M_{20} = 10^5\ \text{A m}^{-1}$, $K_1 = K_2 = 10^{-7}\ \text{H m}^{-1}$, $J_{\text{ex}} = 10^{-5}\ \text{H m}^{-1}$ and $\gamma_2 = 1.8 \times 10^{11}\ \text{s}^{-1}\text{T}^{-1}$. These parameter values are chosen to represent the typical order of magnitude found in FiM but without pertaining to any specific material. The thicknesses are assumed to be $t_H = 10$ nm and $t_F = 5$ nm. For the interfacial conductances, we use the representative values assumed previously [31,35–37] in the absence of available experimental measurements, i.e., $G_r = 2 \times 10^{14}\ \Omega^{-1}\text{m}^{-2}$. Based on these parameters, we compute the ISHE output signal in the absence and presence of a static magnetic field with different FiM properties, including the sublattice magnetization magnitude, gyromagnetic ratio, and Gilbert damping constant.

A. Sublattice magnetization magnitude and gyromagnetic ratio dependence

Experimentally, the sublattice magnetization in a FiM can be altered by changing the sublattice element concentration [18–20] or temperature [21,22], and this flexibility has been utilized to achieve the magnetization compensation point of the FiM. This compensation behavior of the FiM can be captured within our model by varying M_{10} while keeping M_{20} fixed. The ISHE signal is examined with respect to different M_{10}/M_{20} ratios in Fig. 2, where other parameters (e.g., γ_i) are assumed identical for both sublattices. Regardless of whether or not the static magnetic field is present, it can be seen that the magnitude of the ISHE signal increases as the sublattice magnetization approaches the compensation point, and the maximum is achieved at $M_{10}/M_{20} = 1$ (the red curve). To some extent, this behavior corresponds to the experimentally observed enhanced spin torque efficiency [18,23] at compensation as both signals are determined by the interfacial spin current density $\boldsymbol{Q}$. In the absence of a static magnetic field [Fig. 2(a)], only one single resonance peak is observed at $M_{10}/M_{20} = 1$ (the red curve), while for other M_{10}/M_{20} ratios, there are two resonance peaks. This can be explained by considering the expression for the two macrospin resonance frequencies given by Eq. (13), which reduces to one when $M_{10}/M_{20} = 1$, since $\omega_{1\text{eff}} = \omega_{2\text{eff}}$. On the other hand, in the presence of finite static magnetic field, we have $\omega_{1\text{eff}} \neq \omega_{2\text{eff}}$, and therefore resonance occurs at two different frequencies for any value of M_{10}/M_{20} ratios, even at the compensation point where the two resonance peaks have the same amplitude [the red curve in Fig. 2(b)]. Note that $\mu_0 H_0 = 0.1$ T applied here is below the spin-flop field, which ensures the validity of our assumption of small-angle precession about the essentially antiparallel magnetization direction of the two sublattices [38]. In addition, it can be seen in Fig. 2(b) that the resonance frequencies of both modes and the frequency difference between them can be minimized by tuning the FiM to approach its magnetization compensation point. By comparing Figs. 2(a) and 2(b), it can be seen that the inclusion of the static magnetic field slightly decreases the magnitude of the ISHE signal.
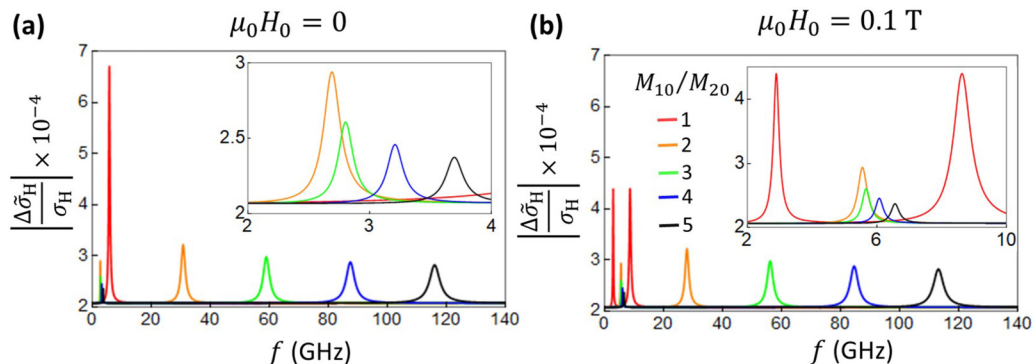
FIG. 2. The normalized ISHE-induced output signal (i.e., effective electric conductivity change of the HM) is plotted as a function of the excitation frequency f with different M_{10}/M_{20} ratios in the absence and presence of a static magnetic field H_0 in (a) and (b), respectively. The insets give the corresponding magnified diagrams of the main panels. The parameters employed are $\alpha_{11} = \alpha_{22} = 0.02$, $\alpha_{12} = \alpha_{21} = 0$ with $\gamma_1 = \gamma_2$.

Next, we investigated the sublattice gyromagnetic ratio dependence of the ISHE signal at the magnetization compensation point (i.e., $M_{10}/M_{20} = 1$) in Fig. 3. In the absence of a static magnetic field [Fig. 3(a)], one single resonance peak is obtained when $\gamma_1/\gamma_2 = 1$ as a result of $\omega_{1\mathrm{eff}} = \omega_{2\mathrm{eff}}$ (the green curve). This peak splits into two normal macrospin resonance peaks for other γ_1/γ_2 ratios. In addition, it can be seen that the ISHE signal amplitude tends to be enhanced with increasing the ratio of γ_1/γ_2.

We delve further into the combined dependence of the ISHE signal on the relative magnetization magnitude and gyromagnetic ratio of the two sublattices. Recalling that $\omega_{1\mathrm{eff}} = \gamma_1(2K_1 M_{10} + J_{\mathrm{ex}} M_{20} + \mu_0 H_0)$ and $\omega_{2\mathrm{eff}} = \gamma_2(2K_2 M_{20} + J_{\mathrm{ex}} M_{10} - \mu_0 H_0)$, it can be concluded that a single resonance peak (i.e., $\omega_{1\mathrm{eff}} = \omega_{2\mathrm{eff}}$) would ensue if both M_{i0} and γ_i are symmetric for the two sublattices in the absence of a static magnetic field, otherwise two normal resonance peaks are generally observed. On the other hand, in the presence a static magnetic field, having two resonance peaks with the same amplitude would indicate identical values of both M_{i0} and γ_i for the two sublattices. In general, the number, frequency and relative amplitude of the resonance peaks in the ISHE spectrum can provide a means to probe the sublattice asymmetry in the saturation magnetization and gyromagnetic coefficient of the FiM sublattices. In addition, since the

frequency difference between the two resonance peaks determined by ($\omega_{1\mathrm{eff}} - \omega_{2\mathrm{eff}}$) is minimized in the absence of the static magnetic field, it may be easier to experimentally detect both resonance peaks by applying a smaller static magnetic field.

B. Gilbert damping dependence

Experimentally, the damping strongly depends on the material and geometrical properties of the fabricated bilayer sample, e.g., the layer thickness, interface properties, etc. An enhanced magnetic damping can also be expected by engineering increased interface roughness or atomic diffusion via elevated annealing temperature [39]. On the other hand, adding an ultrathin interlayer made of Cu (or Al) may provide an alternative way to tune the Gilbert damping by changing the interlayer thickness [39,40]. In this section, we first investigate the Gilbert damping type dependence of the ISHE signal as plotted in Fig. 4. We consider the magnetization compensation point ($M_{10} = M_{20}$) and symmetric gyromagnetic ratio ($\gamma_1 = \gamma_2$). For the previous calculations (i.e., Figs. 2 and 3), we assume $\alpha_{11} = \alpha_{22} = 0.02$ and $\alpha_{12} = \alpha_{21} = 0$, i.e., the FiM possesses the same on-site-sublattice damping while the cross-sublattice damping terms are treated as negligible. We use this damping configuration as the reference case in Fig. 4
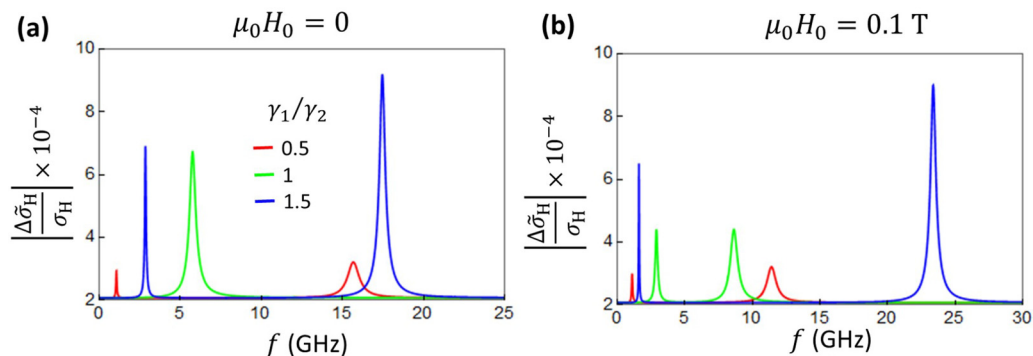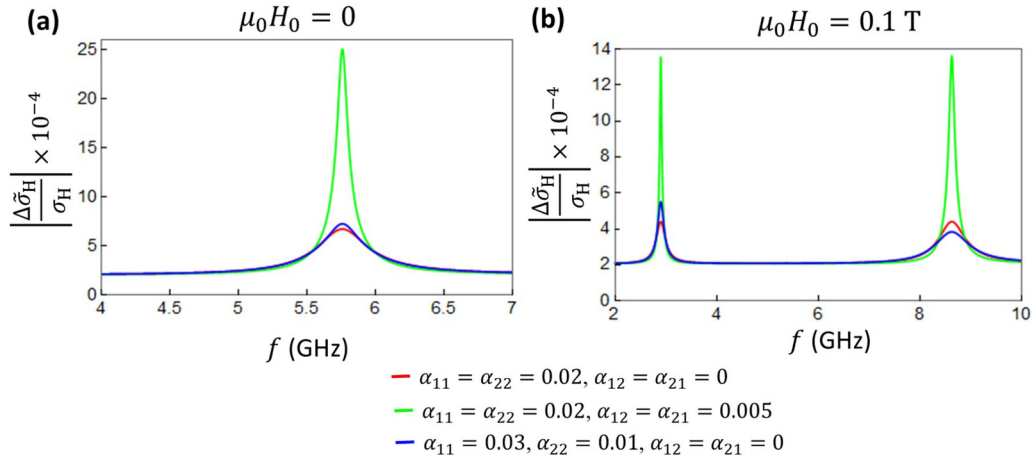

FIG. 3. The normalized ISHE-induced output signal (i.e., effective electric conductivity change of the HM) at the magnetization compensation point is depicted as a function of the excitation frequency f with different γ_1/γ_2 ratios in the absence and presence of a static magnetic field H_0 in (a) and (b), respectively. The damping parameters employed are the same as for Fig. 2.

FIG. 4. The normalized ISHE-induced output signal (i.e., effective electric conductivity change of the HM) at the magnetization compensation point is depicted as a function of the excitation frequency f with different damping types in the absence and presence of a static magnetic field H_0 in (a) and (b), respectively. The red curves give the results for the symmetric on-site-sublattice damping and neglecting the cross-sublattice damping terms. The other two cases of finite cross-sublattice damping terms and asymmetric on-site-sublattice damping are represented by the green and blue curves, respectively. Here $\gamma_1 = \gamma_2$ is employed.

(depicted by the red curves). However, recent theoretical proposals on spin pumping in two-sublattice magnets [28,32,41] suggest an important role for the previously disregarded cross-sublattice terms in Gilbert damping. Within our model, it can be seen that the introduction of the cross-sublattice damping terms substantially modifies the magnitude of the ISHE signal, while their effect on the resonance frequencies are negligible, as shown by the green curves. In addition, we consider the asymmetry of the on-site-sublattice damping (the blue curves), which also modifies the peak amplitude but to a much lesser extent compared to the cross-sublattice damping. Its effect on the resonance frequencies are likewise negligible. This validates our assumption of negligible dependence of ω_{res} on the damping parameters in our derivation of Eq. (13). Interestingly, in the presence of a static magnetic field [Fig. 4(b)], the two resonance peaks differ in amplitude (the blue curve) in the case of asymmetric on-site-sublattice damping. They have the same amplitude for the case of symmetric on-site-sublattice damping, as discussed before. According to the previous experimental results based on the element-resolved x-ray ferrimagnetic resonance [42], the same value of the on-site-sublattice damping constants in FiM would be expected. Therefore, the proposed detectable ISHE signal can potentially be used as an additional aproach to check the symmetry of the sublattice damping constants.

Next, we further examine the Gilbert damping constant dependence of the ISHE signal. The resonance peak amplitude of the ISHE signal as a function of the on-site-sublattice damping constant is plotted in Fig. 5(a), where $\alpha_{11} = \alpha_{22}$ is assumed for simplicity. Note here we are considering the case that both M_{i0} and γ_i are identical for the two sublattices in the absence of a static magnetic field, and therefore only one single resonance peak appears. Surprisingly, a sharp peak in the resonance amplitude is obtained as α_{11} is varied, with the maximum occurring at $\alpha_{11} \sim 0.014$. Compared with $\alpha_{11} = 0.02$ used in the previous simulations, the amplitude maximum achieved at $\alpha_{11} \sim 0.014$ is drastically enhanced by two orders of magnitude. Analytically, the optimal value

of on-site-sublattice damping of $\alpha_{11} \sim 0.014$ can be obtained by setting the determinant of $\mathcal{F}$ as zero at $\omega = \omega_{\text{res}}$, which corresponds to the maximum interfacial spin current density Q [see Eqs. (20) and (21)]. In Fig. 5(b), we plot the ISHE signal as a function of the excitation frequency f with several α_{11} values, which further validates the maximum of the peak amplitude appears at $\alpha_{11} \sim 0.014$. Interestingly, the large enhancement in the amplitude is accompanied by little or no change in the resonance frequency. At this optimal α_{11}, the resonance amplitude maximum can be further amplified by tuning the cross-sublattice damping parameter α_{12}, as shown in Figs. 5(c) and 5(d). We find a sharp peak at $\alpha_{12} \sim 1.5 \times 10^{-4}$, at which a further enhancement of two orders of magnitude is achieved compared with the case that only the on-site-sublattice damping exists. This ultrasensitive dependence of the ISHE signal on the on-site-sublattice as well as cross-sublattice damping parameters provides an insight into these damping coefficients, which are usually not easily accessible by other experimental techniques. Conversely, these sharp enhancements of ISHE at specific values of α_{11} and α_{12} indicate that the injected spin current, and hence the spin torque efficiency to a FiM layer, can be significantly enhanced by optimizing the damping parameters. In addition, the signal enhancement is generally accompanied with the decrease of the ferrimagnetic resonance linewidth, both of which are correlated to the determinant of $\mathcal{F}$. However, due to the complexity of $\mathcal{F}$ which includes the matrix inverse $\mathcal{M}^{-1}$, the FMR linewidth could not be expressed in a compact analytical form in terms of the explicit damping constants within $\mathcal{M}$ matrix. On the other hand, in the presence of a static magnetic field, the single resonance peak in Fig. 5 would split into two, and therefore the optimal damping has to be obtained separately for each peak. However, in order to avoid spin-flop transition, the applied magnetic field has to be small. Thus, there would be negligible difference of the optimal damping constants for the two peaks and the optimal damping constants obtained in the absence of the static magnetic field (Fig. 5) would still be valid.
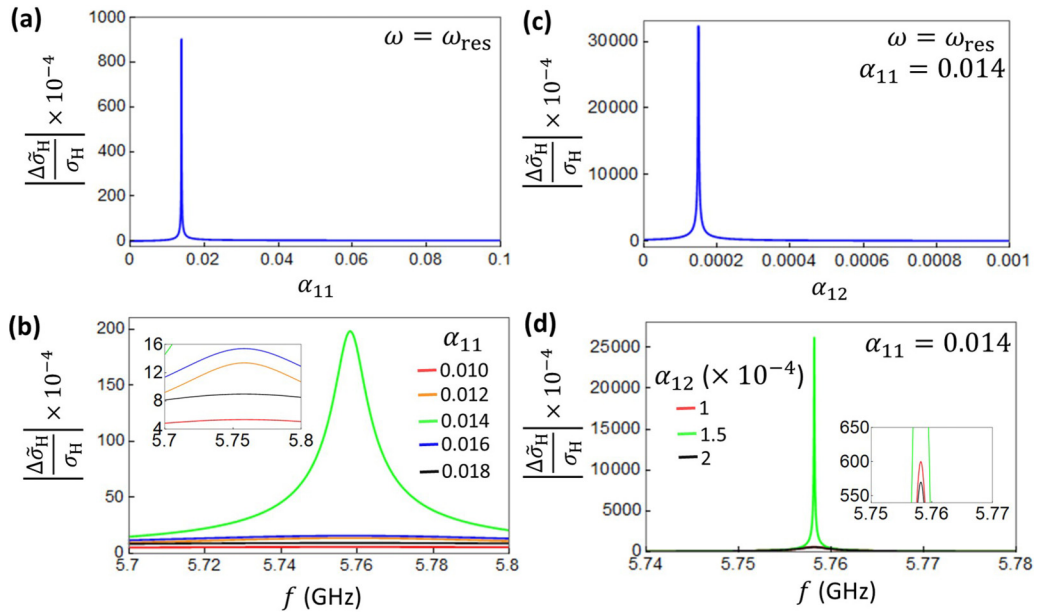
FIG. 5. The peak amplitude of the normalized ISHE-induced output signal (i.e., effective electric conductivity change of the HM) under the resonance condition is depicted as a function of the on-site-sublattice damping α_{11} in (a) and of the cross-sublattice damping α_{12} in (c), respectively. The normalized ISHE-induced output signal (i.e., effective electric conductivity change of the HM) is depicted as a function of the excitation frequency f with different α_{11} values in (b) and different α_{12} values in (d), respectively, where the insets give the corresponding magnified diagrams of the main panels. $\alpha_{12} = \alpha_{21} = 0$ is employed in (a) and (b), and $\alpha_{11} = \alpha_{22} = 0.014$ is employed in (c) and (d). In all panels, $M_{10} = M_{20}$ and $\gamma_1 = \gamma_2$ are utilized.

Finally, based on all above numerical simulations, it can be seen that each resonance peak of the ISHE signal has a symmetric line shape. Although the Oersted field generated by the oscillating current can give an antisymmetric spectrum [8], it is negligible compared with the SHE contribution in our numerical simulation. Our model is based on the macrospin approximation, i.e., we assume the magnetization configuration to be spatially invariant. Despite this simplifying assumption, our model reveals unexpected behavior especially with regard to the damping parameters. We envisage even richer behavior with further investigations which include the excitation of spatially varying modes, such as standing spin waves [43], from which the higher-energy resonance modes may appear. In addition, the rectified DC voltage should be nonzero in our proposed FiM/HM structure with perpendicular configuration, unlike the zero DC signal based on ferromagnets [44,45], which can provide an avenue for experimental verification. Last, the compensated FiM mimics an AFM to some extent except for different material parameter values. Accounting for the sublattice symmetry of the AFMs, both $\gamma_1/\gamma_2 = 1$ and $M_{10}/M_{20} = 1$ should be utilized while the damping can assume different values for the two sublattices [28]. Under these assumptions, the drastic ISHE signal enhancement with the optimal damping constants would still be applicable.

IV. CONCLUSION

In this work, we examined the ferrimagnetic resonance induced by the SHE in a FiM/HM bilayer with an oscillating electric current. The FiM resonance dynamics induces a spin-pumped back current into the HM layer, which translates to a measurable signal via the ISHE. A phenomenological theory is presented to relate the output spectrum of the ISHE signal (i.e., effective electric conductivity change of the HM), which couples the spin transport in the HM to the magnetization dynamics in the FiM insulator. Our calculated results show that the detectable ISHE output spectrum is strongly influenced by the magnetic parameters of the FiM. As expected, there is a large enhancement of the ISHE signal at the compensation point of the FiM. Furthermore, the frequencies and relative amplitudes of the peaks in the ISHE spectrum can be correlated to the asymmetry in the magnetic properties of the FiM sublattices. Interestingly, the ISHE output can be increased by several orders of magnitude by tuning the on-site-sublattice and cross-sublattice damping coefficients. Our analysis shows that one can use the FiM-HM bilayer system to effectively probe the magnetic parameters of the FiM sublattices by exciting the bilayer with an oscillating current and analyzing the resulting ISHE spectrum. Conversely, the drastically enhanced ISHE signal with appropriate tuning of the damping parameters suggests a possible means to substantially improve the spin torque efficiency in FiM-based heterostructures.

[1] L. Liu, T. Moriyama, D. C. Ralph, and R. A. Buhrman, Phys. Rev. Lett. **106**, 036601 (2011).

[2] T. Tanaka, H. Kontani, M. Naito, T. Naito, D. S. Hirashima, K. Yamada, and J. Inoue, Phys. Rev. B **77**, 165117 (2008).

[3] L. Liu, C.-F. Pai, Y. Li, H. Tseng, D. Ralph, and R. Buhrman, Science **336**, 555 (2012).

[4] C.-F. Pai, L. Liu, Y. Li, H. Tseng, D. Ralph, and R. Buhrman, Appl. Phys. Lett. **101**, 122404 (2012).

[5] Y.-T. Chen, S. Takahashi, H. Nakayama, M. Althammer, S. T. B. Goennenwein, E. Saitoh, and G. E. W. Bauer, Phys. Rev. B **87**, 144411 (2013).

[6] S. Cho, S. H. Baek, K. D. Lee, Y. Jo, and B. G. Park, Sci. Rep. **5**, 14668 (2015).

[7] H. Nakayama, M. Althammer, Y.-T. Chen, K. Uchida, Y. Kajiwara, D. Kikuchi, T. Ohtani, S. Geprägs, M. Opel, S. Takahashi, R. Gross, G. E. W. Bauer, S. T. B. Goennenwein, and E. Saitoh, Phys. Rev. Lett. **110**, 206601 (2013).

[8] T. Chiba, G. E. W. Bauer, and S. Takahashi, Phys. Rev. Appl. **2**, 034003 (2014).

[9] M. Schreier, T. Chiba, A. Niedermayr, J. Lotze, H. Huebl, S. Geprägs, S. Takahashi, G. E. W. Bauer, R. Gross, and S. T. B. Goennenwein, Phys. Rev. B **92**, 144411 (2015).

[10] J. Sklenar, W. Zhang, M. B. Jungfleisch, W. Jiang, H. Chang, J. E. Pearson, M. Wu, J. B. Ketterson, and A. Hoffmann, Phys. Rev. B **92**, 174406 (2015).

[11] C. He, A. Navabi, Q. Shao, G. Yu, D. Wu, W. Zhu, C. Zheng, X. Li, Q. L. He, S. A. Razavi, K. L. Wong, Z. Zhang, P. K. Amiri, and K. L. Wang, Appl. Phys. Lett. **109**, 202404 (2016).

[12] Q. Zhang, X. Fan, H. Zhou, W. Kong, S. Zhou, Y. Gui, C.-M. Hu, and D. Xue, Appl. Phys. Lett. **112**, 092406 (2018).

[13] A. Kimel, A. Kirilyuk, A. Tsvetkov, R. Pisarev, and T. Rasing, Nature (London) **429**, 850 (2004).

[14] T. Jungwirth, X. Marti, P. Wadley, and J. Wunderlich, Nat. Nanotechnol. **11**, 231 (2016).

[15] P. Wadley, B. Howells, J. Železný, C. Andrews, V. Hills, R. P. Campion, V. Novák, K. Olejník, F. Maccherozzi, S. S. Dhesi, S. Y. Martin, T. Wagner, J. Wunderlich, F. Freimuth, Y. Mokrousov, J. Kuneš, J. S. Chauhan, M. J. Grzybowski, A. W. Rushforth, K. W. Edmonds *et al.*, Science **351**, 587 (2016).

[16] J. Li, C. B. Wilson, R. Cheng, M. Lohmann, M. Kavand, W. Yuan, M. Aldosary, N. Agladze, P. Wei, M. S. Sherwin, and J. Shi, Nature (London) **578**, 70 (2020).

[17] P. Vaidya, S. A. Morley, J. van Tol, Y. Liu, R. Cheng, A. Brataas, D. Lederman, and E. Del Barco, Science **368**, 160 (2020).

[18] R. Mishra, J. Yu, X. Qiu, M. Motapothula, T. Venkatesan, and H. Yang, Phys. Rev. Lett. **118**, 167201 (2017).

[19] M. Binder, A. Weber, O. Mosendz, G. Woltersdorf, M. Izquierdo, I. Neudecker, J. R. Dahn, T. D. Hatchard, J.-U. Thiele, C. H. Back, and M. R. Scheinfein, Phys. Rev. B **74**, 134404 (2006).

[20] S. A. Siddiqui, J. Han, J. T. Finley, C. A. Ross, and L. Liu, Phys. Rev. Lett. **121**, 057701 (2018).

[21] L. Caretta, M. Mann, F. Büttner, K. Ueda, B. Pfau, C. M. Günther, P. Hessing, A. Churikova, C. Klose, M. Schneider, D. Engel, C. Marcus, D. Bono, K. Bagschik, S. Eisebitt, and G. S. Beach, Nat. Nanotechnol. **13**, 1154 (2018).

[22] Y. Hirata, D. H. Kim, T. Okuno, T. Nishimura, D. Y. Kim, Y. Futakawa, H. Yoshikawa, A. Tsukamoto, K. J. Kim, S. B. Choe, and T. Ono, Phys. Rev. B **97**, 220403(R) (2018).

[23] J. Finley and L. Liu, Phys. Rev. Appl. **6**, 054001 (2016).

[24] K. Cai, Z. Zhu, J. M. Lee, R. Mishra, L. Ren, S. D. Pollard, P. He, G. Liang, K. L. Teo, and H. Yang, Nat. Electron. **3**, 37 (2020).

[25] Q. Shao, A. Grutter, Y. Liu, G. Yu, C. Y. Yang, D. A. Gilbert, E. Arenholz, P. Shafer, X. Che, C. Tang, M. Aldosary, A. Navabi, Q. L. He, B. J. Kirby, J. Shi, and K. L. Wang, Phys. Rev. B **99**, 104401 (2019).

[26] S. Crossley, A. Quindeau, A. Swartz, E. Rosenberg, L. Beran, C. Avci, Y. Hikita, C. Ross, and H. Hwang, Appl. Phys. Lett. **115**, 172402 (2019).

[27] M. B. Jungfleisch, W. Zhang, J. Sklenar, J. Ding, W. Jiang, H. Chang, F. Y. Fradin, J. E. Pearson, J. B. Ketterson, V. Novosad, M. Wu, and A. Hoffmann, Phys. Rev. Lett. **116**, 057601 (2016).

[28] A. Kamra, R. E. Troncoso, W. Belzig, and A. Brataas, Phys. Rev. B **98**, 184402 (2018).

[29] F. Keffer and C. Kittel, Phys. Rev. **85**, 329 (1952).

[30] R. K. Wangsness, Phys. Rev. **91**, 1085 (1953).

[31] V. Sluka, Phys. Rev. B **96**, 214412 (2017).

[32] A. Kamra and W. Belzig, Phys. Rev. Lett. **119**, 197201 (2017).

[33] M. Weiler, M. Althammer, M. Schreier, J. Lotze, M. Pernpeintner, S. Meyer, H. Huebl, R. Gross, A. Kamra, J. Xiao, Y. T. Chen, H. J. Jiao, G. E. W. Bauer, and S. T. B. Goennenwein, Phys. Rev. Lett. **111**, 176601 (2013).

[34] M. Obstbaum, M. Härtinger, H. G. Bauer, T. Meier, F. Swientek, C. H. Back, and G. Woltersdorf, Phys. Rev. B **89**, 060407(R) (2014).

[35] N. Chung, M. Jalil, and S. Tan, J. Phys. D: Appl. Phys. **42**, 195502 (2009).

[36] C. Sun, Z. B. Siu, S. G. Tan, H. Yang, and M. B. Jalil, J. Appl. Phys. **123**, 153901 (2018).

[37] C. Sun, J. Deng, S. M. Rafi-Ul-Islam, G. Liang, H. Yang, and M. B. A. Jalil, Phys. Rev. Appl. **12**, 034022 (2019).

[38] S. Blundell, Am. J. Phys. **71**, 94 (2003).

[39] Z. Zhu, G. Wu, Y. Ren, S. Lou, Q. Jin, and Z. Zhang, Appl. Phys. Lett. **116**, 182407 (2020).

[40] D. Zhang, M. Li, L. Jin, C. Li, Y. Rao, X. Tang, and H. Zhang, ACS Appl. Electron. Mater. **2**, 254 (2020).

[41] Q. Liu, H. Y. Yuan, K. Xia, and Z. Yuan, Phys. Rev. Materials **1**, 061401 (2017).

[42] G. Boero, S. Mouaziz, S. Rusponi, P. Bencok, F. Nolting, S. Stepanow, and P. Gambardella, New J. Phys. **10**, 013011 (2008).

[43] Ø. Johansen, H. Skarsvåg, and A. Brataas, Phys. Rev. B **97**, 054423 (2018).

[44] T. Chiba, M. Schreier, G. E. Bauer, and S. Takahashi, J. Appl. Phys. **117**, 17C715 (2015).

[45] L. Bai, P. Hyde, Y. S. Gui, C.-M. Hu, V. Vlaminck, J. E. Pearson, S. D. Bader, and A. Hoffmann, Phys. Rev. Lett. **111**, 217602 (2013).